Seven-Sensor Fast-Response Probe for Full-Scale Wind Turbine Flowfield Measurements

M. Mansour
G. Kocer
C. Lenherr
N. Chokani
R. S. Abhari

Department of Mechanical and Process Engineering,
Laboratory for Energy Conversion,
ETH Zürich,
Zurich 8092, Switzerland

The unsteady wind profile in the atmospheric boundary layer upstream of a modern wind turbine is measured. The measurements are accomplished using a novel measurement approach that is comprised of an autonomous uninhabited aerial vehicle (UAV) that is equipped with a seven-sensor fast-response aerodynamic probe (F7S-UAV). The autonomous UAV enables high spatial resolution (~6.3% of rotor diameter) measurements, which hitherto have not been accomplished around full-scale wind turbines. The F7S-UAV probe developed at ETH Zurich is the key-enabling technology for the measurements. The time-averaged wind profile from the F7S-UAV probe is found to be in very good agreement to an independently measured profile using the UAV. This time-averaged profile, which is measured in moderately complex terrain, differs by as much as 30% from the wind profile that is extrapolated from a logarithmic height formula; therefore, the limited utility of extrapolated profiles, which are commonly used in site assessments, is made evident. The time-varying wind profiles show that at a given height, the velocity fluctuations can be as much as 44% of the time-averaged velocity, therefore indicating that there are substantial loads that may impact the fatigue life of the wind turbine's components. Furthermore, the shear in the velocity profile also subjects the fixed pitch blade to varying incidences and loading. Analysis of the associated velocity triangles indicates that the sectional lift coefficient at midspan of this modern turbine would vary by 12% in the measured time-averaged wind profile. These variations must be accounted in the structural design of the blades. Thus, the measurements of the unsteady wind profile accomplished with this novel measurement system demonstrate that it is a cost effective complement to the suite of available site assessment measurement tools.
[DOI: 10.1115/1.4002781]

1 Introduction

Over the past decade, the global wind industry has experienced exponential growth; the annual increase in installed capacity averages 29%. In 2009, the new installed wind capacity led all new electric generating capacity (even ahead of new natural gas), accounting for 39% of all new electric generating capacity, in both the EU and the USA, respectively, the world's leading regional and national markets for wind power. The growth of wind generated electricity is driven by its many benefits including no CO_2 emissions, no water consumption for electricity generation, security of energy supply through increasingly diversified electrical energy mix, and major economic impact (in 2009, €42 billion new power generation equipment and approximately 500,000 jobs in the global wind industry). The continued rapid development of wind energy projects requires improved approaches to site assessment, such that the acquisition time of the wind resource is reduced for wind farm developers and the placement of wind turbines is optimized for wind farm operators.

Until now, site assessment is most commonly performed using a mast-mounted cup anemometer, which offers a robust and simple solution [1]. Due to the rapid increase in turbine size over the last years, with typical hub heights often exceeding 90 m, the mast-mounted cup anemometers have shown their limits. The erection of higher mast-anemometer leads to onerous installation and maintenance costs for the developer of a wind energy project. Moreover, this technique offers only a few discrete points of measurements, which are insufficient to assess the wind profile accurately, and thus the expected annual energy yield for wind turbines that are located in moderately and highly complex terrains. A further limitation is that the current understanding of flows around full-scale wind turbines is largely derived from point measurements obtained from a few widely scattered masts. These point measurements are insufficient to improve the understanding and comprehension of interaction between a large modern wind turbine (rotor diameter 80–120 m) and a turbulent atmospheric boundary flow (thickness 200–1500 m). A more detailed understanding of the turbulent flows upstream, as well as downstream, of the wind turbines is required. Recently, substantial efforts have focused on the use of light detection and ranging (LIDAR) measurement systems in wind energy applications [2–4]. However, short range LIDAR profilers are limited to observations up to 200 m along a single line, and are therefore not cost effective solutions to detail the 3D flowfield around wind turbines. To overcome this limitation, 3D "windscanners" have been developed either by having a system that scans the transmitted beam over 360 deg in azimuth [5] and for various heights or by having a set of three steerable Doppler LIDARs [6]. Their drawback is the prohibitive system cost and limited flexibility in transportation and set-up.

The objective of this paper is to assess the use of an instrumented UAV to provide wind measurements in wind energy projects. This assessment is part of the recently developed multifaceted wind energy program at ETH Zurich. The components of this program include econometric modeling, computational fluid dynamic modeling, subscale wind turbine experiments, and full-scale experiments on wind turbines. The purpose of the subscale and full-scale experiments is to provide detailed flowfield data that can be used to enhance and validate the computational models. Therefore, the specific goal of the current project is to develop a light, mobile, cost effective measurement system that can be used either to provide time-resolved wind measurements around

Contributed by the International Gas Turbine Institute (IGTI) of ASME for publication in the JOURNAL OF ENGINEERING FOR GAS TURBINES AND POWER. Manuscript received May 18, 2010; final manuscript received May 20, 2010; published online April 5, 2011. Editor: Dilip R. Ballal.

full-scale wind turbine or complementary wind profile measurements for site assessment. UAVs fulfill the requirement of being lightweight, mobile, and cost effective and have proven their reliability in several meteorological measurement campaigns [7,8]. In order to provide wind measurements on such a platform, the key enabler is the fast-response aerodynamic probe technology that has been developed at ETH Zurich for turbomachinery applications. The adaptation, development, integration, and demonstration of this technology for use on a UAV to provide time-resolved wind profile measurements in full-scale wind turbine applications is the subject of this paper. In the subsequent sections, the design and calibration of the seven-sensor fast-response aerodynamic probe (7S-FRAP), as well as its integration in the UAV are presented in detail. Then, wind profile measurement results performed upstream of a wind turbine are presented and discussed.

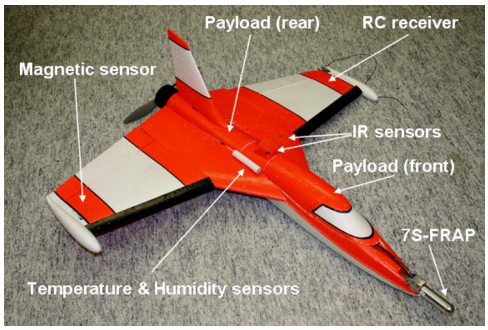

Fig. 1 Autonomous time-resolved wind measurement aircraft based on the model airframe Funjet

2 7S-FRAP Technique

The principal component for time-resolved wind measurements is the 7S-FRAP. The probe is based on previous turbomachinery applications in the Laboratory for Energy Conversion at the Swiss Federal Institute of Technology Zürich. Detailed aspects and applications of FRAP technology were described by Kupferschmied et al. [9], Pfau et al. [10], Porreca et al. [11], and Mansour et al. [12], however, specific information for the current wind energy application are detailed below.

2.1 Requirements. The principal requirements for the probe were the capability to measure wind (speed, direction, and turbulence parameters) in the atmospheric boundary layer and downstream of a wind turbine. Thus, measurements in low dynamic head (0–10 mbars), over large flow angles ($\leq$70 deg), and with large bandwidth ($\leq$1 kHz) are required. A major challenge was to accomplish these with a measurement system that did not exceed the payload and autonomous flight limitations of the UAV, which was the chosen platform for high resolution flowfield measurements of full-scale wind turbines. Moreover, the probe and sensor packaging needed to be robust, such that they can be reliably operated on a UAV.

2.2 Sensor Packaging. The sensing elements of the 7S-FRAP employ miniature pressure sensor dies (Intersema MS-7505-D); this sensor is designed for low pressure applications ($\leq$50 mbars) that have stringent requirements on resolution and accuracy.

The sensor packaging and bonding techniques are derived from micro-electro-mechanical system (MEMS) technology. These packaging and the bonding techniques ensure optimal spatial resolution, measurement bandwidth, and protection of the sensors in harsh weather conditions. Moreover, the gluing and bonding techniques employed in the present design provided a high degree of reliability and low disturbance to the sensors as the probe can experience large temperature and pressure fluctuations.

The miniature silicon piezoresistive chip is glued onto a socket using silicon glue with very low E-modulus. The silicon glue is based on an inorganic ground structure, which offers large temperature range of operation ($-90-200\,^{\circ}$C) and is highly resistant to corrosive media. Thus, the thermomechanical stresses are minimized. The photopolymer socket is encapsulated into a threaded casing of 5.5 mm in diameter. The treated casing enables a repeatable fixation of a sensor in the probe tip, as well as the quick replacement of the sensor in case of a failure.

2.3 Probe Design. The 7S-FRAP consists of a 20 mm hemispherical probe head that is comprised of seven fast-response pressure sensors installed beneath the pressure taps. The sensing holes have a diameter of 1.3 mm, which is less than one-twelfth of the probe diameter, ensuring negligible influence on the aerocalibration [13]. As the total and static pressures occur on the surface of a hemispherical probe at flow angles equal to 0 deg and about 45 deg, respectively, the probe incorporates the surface pressure tapings at these positions with respect to the probe shaft axis. The volume and the length of pressure taps of the probe tip body are minimized, as these dimensions have a significant impact on the probe aerodynamics and measurement bandwidth. The reduction of the pressure tap volume is a key parameter to yield a high frequency measurement bandwidth as the eigenfrequency of the pneumatic cavity will affect the pressure sensor dynamic response. This issue is further discussed below in the dynamic calibration section.

The probe tip is installed on a cylindrical shaft to give an overall probe length of 70 mm, which minimizes the potential field effect of the UAV on the probe's flowfield. The shaft has a squared-end, which enables the repeatable installation of the probe on the UAV.

2.4 Uninhabited Aerial Vehicle. In order to perform full-scale wind turbine measurements, the 7S-FRAP probe is installed on an uninhabited aerial vehicle (UAV) (Fig. 1).

The "Funjet" airframe, manufactured by Multiplex, is of a pusher-prop configuration. The airframe is made of a very durable and easily repairable expanded polypropylene construction. It has a wingspan of 800 mm and weighs 900 g when fully instrumented. The propeller is driven by a brushless electric motor in order to reduce the vibrations that may affect the on-board sensors. As the airframe has limited payload bay area, significant effort has been put into the development of compact and light electronics and avionics. The system is powered with a lithium battery that provides flight autonomy of approximately 25 min at a cruise speed of 15 m/s.

Since remote pilot control is only possible within the range of sight and does not offer accurate and repeatable flight paths, the fully autonomous flight control system Paparazzi was used. Paparazzi is an open-source autopilot system oriented toward inexpensive autonomous aircraft [14,15]. The Paparazzi system includes an on-board processor with its required sensors, autopilot software, a ground control station, and a simulation environment to prepare and test the flight plans. The attitude is measured using a set of infrared thermopiles that sense the differential temperature between sky and ground. The altitude, the position, as well as the ground speed are derived using a global positioning system (GPS) receiver. The GPS provides a horizontal and vertical position accuracy of $\pm$2.5 m and $\pm$5 m, respectively. The ground speed accuracy is $\pm$0.1 m/s at 30 m/s, with an error on the course heading of 0.5 deg.

In addition to the autopilot sensors, the UAV is equipped with sensors that are required to process the measurements from the seven-sensor fast-response probe. A magnetic sensor is installed to the UAV's sideslip angle. The magnetic sensor is placed at the tip of the wing fuselage to reduce distortion effects of the on-board electronics. The atmospheric pressure, used as the reference pressure for the fast-response differential pressure sensors of the 7S-FRAP, is measured via an absolute pressure sensor located in the rear compartment of the payload bay. In order to accurately char-

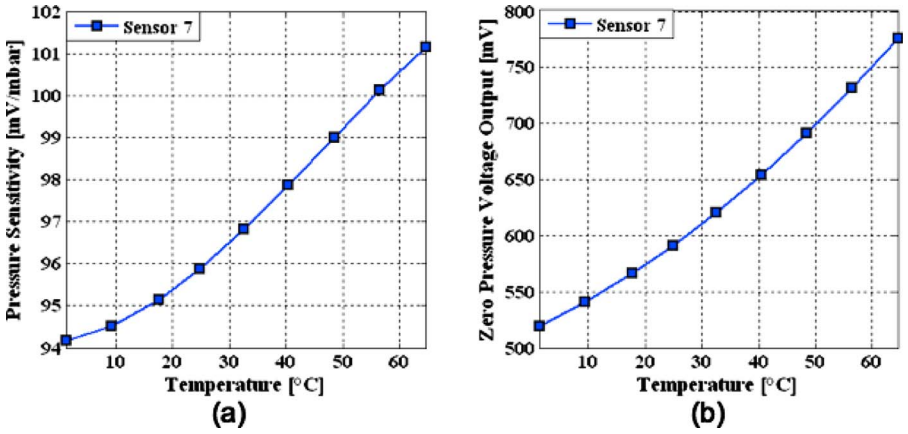

Fig. 2 (*a*) **Pressure sensitivity versus applied temperature and** (*b*) **zero pressure offset versus temperature**

acterize the atmospheric boundary layer profile and the work rate obtainable from measured wind profile, a sensor mounted external to the airframe measures temperature and humidity of the air.

The 7S-FRAP probe pressure signals are acquired simultaneously with 24 bit resolution over a differential analog input range of ± 2.2 V and at a data sampling rate of 250 Hz. The remaining on-board sensors are acquired with resolutions ranging from 12 bits to 16 bits. The data are stored in binary format on an on-board multimedia flash card.

3 Results

3.1 Static Calibration. The piezoresistive sensors are calibrated over a pressure and temperature range of 1–30 mbars and 1–65°C, respectively. For the measurements, a fifth-order polynomial interpolation, Eqs. (1) and (2) are used to determine the pressure and temperature from the measured sensor signals.

The measured sensitivities of the pressure sensor after amplification are 98 mV/mbars and 135 mV/K for the pressure signal and the temperature signal, respectively. The noise on the pressure signal reduces the resolution of the analog-to-digital converter to 19 bit effective, which provides a differential pressure measurement resolution of $\pm 8.6 \times 10^{-3}$ Pa. The calibration model exhibits an average standard deviation compared with the measured data of ± 2.27 Pa and ± 0.14 K, which corresponds to an error of less than 0.075% and 0.018% over the full calibration range of the probe.

$$p(U,U_e) = \sum_{i=0}^{m} \sum_{j=0}^{n} K_{p_{i,j}} U^i U_e^j \tag{1}$$

$$T(U,U_e) = \sum_{i=0}^{m} \sum_{j=0}^{n} K_{T_{i,j}} U^i U_e^j \tag{2}$$

The output signal U is weakly temperature dependent while the excitation signal U_e is decoupled from the pressure. However, the effect of temperature on the pressure sensitivity, see Fig. 2(*a*) and the zero pressure offset, which is the pressure signal output at zero applied pressure, see Fig. 2(*b*), is not negligible. The pressure signal output experiences 7.4% and 47% increase in pressure sensitivity and zero pressure output, respectively, when temperature varies from 1°C to 65°C. It can also be observed that the response to temperature variations is nonlinear. Therefore, the sensors must be calibrated over the full range of intended temperature use.

3.2 Aerodynamic Calibration. The seven-sensor probe design is used to measure the wind over the high flow angle variations present in the turbulent boundary layer and in the wake of wind turbines. Figure 3 shows (a) the definition of the flow angles and (b) the arrangement of the pressure taps. The probe is used in a non-nulling fashion and the pressure information from the seven sensors is combined to compute four pressure coefficients, representing the local yaw angle ψ, pitch angle θ, total pressure P_o, and dynamic pressure q. This information is then used to derive the local velocity vector $\boldsymbol{v}$.

At low flow angles, the flow remains attached over the entire surface of the probe and the central port ($n=7$) has the highest pressure. Therefore, the pressures measured by all seven sensors are used to determine the flow conditions. However, at high flow angles, the flow separates on the leeward side of the probe and an off-center pressure sensor ($n=1-6$) has the highest pressure. In this case, only a subset of the seven pressure sensors is used to determine the flow conditions, based on the sensor reading the highest pressure and the sensors that are adjacent to it. The difference between high and low flow angles leads to a sectoring scheme, which is employed in the current paper, as shown in Fig.

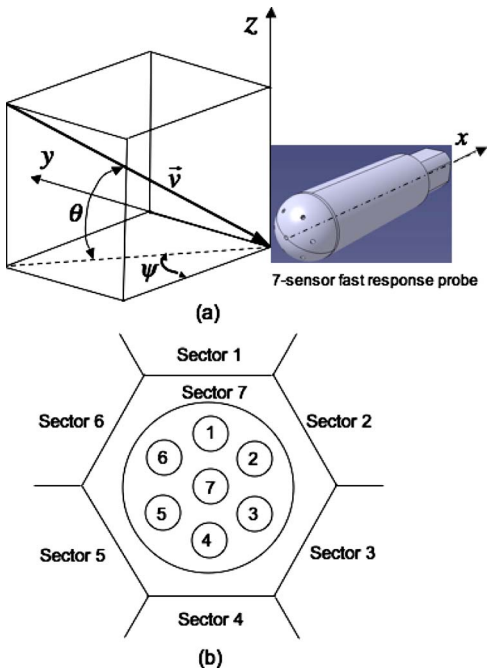

Fig. 3 (*a*) **Flow angles convention and** (*b*) **pressure taps numbering and sectoring scheme**

3(*b*).

The aerocalibration of the probe was made in the fully automated freejet facility at ETHZ. A detailed description of the facility can be found in Ref. [9]. The probe is installed on a three axis traversing system (lateral motion, yaw angle, and pitch angle motion) in order to rotate the probe relative to the fixed jet. The automatic calibration procedure follows a predefined measurement grid for different probe yaw and pitch angles. For the low angle range, the set of calibration data is taken on a homogenous grid that covers ±30 deg in yaw and pitch angles, for a Mach number of 0.07, that corresponds to a velocity of 25 m/s.

Following an approach similar to that of Zilliac [16], a pitch angle coefficient C_θ is used to represent the local pitch angle θ and a tangential pressure-difference coefficient C_ψ is used to represent local yaw angle ψ. Similar coefficients C_o and C_q are used to derive the total pressure and dynamic pressure, respectively. These coefficients are defined for low angles corresponding to sector 7 as follows:

$$C_{\theta,7} = \frac{2(P_4 - P_1) + (P_3 - P_6) - (P_2 - P_5)}{2(P_7 - \bar{P}_7)} \tag{3}$$

$$C_{\psi,7} = \frac{(P_3 - P_6) + (P_2 - P_5)}{\sqrt{3}(P_7 - \bar{P}_7)} \tag{4}$$

$$C_{o,7} = \frac{P_7 - P_o}{P_7 - \bar{P}_7} \tag{5}$$

$$C_{q,7} = \frac{P_7 - \bar{P}_7}{q} \tag{6}$$

$$\bar{P}_7 = \frac{1}{6}\sum_{n=1}^{6} P_n \tag{7}$$

The polynomial curve-fit method of Gallington [17] is applied to the calibration data. Four sets of calibration coefficients are derived for the four flow properties (ψ, θ, C_o, C_q). The polynomial calibration coefficients $k_{ij\psi}$ and $k_{ij\theta}$, used to derive yaw and pitch flow angles, result from the solution of this set of linear equations using a least-squares tenth-order polynomial approximation, as shown in Eqs. (8) and (9)

$$\psi = \sum_{i=0}^{n}\sum_{j=0}^{m} k_{ij\psi} C_\psi^i C_\theta^j \tag{8}$$

$$\theta = \sum_{i=0}^{n}\sum_{j=0}^{m} k_{ij\theta} C_\psi^i C_\theta^j \tag{9}$$

A similar procedure as for the flow angles is applied to the pressure measurements in order to derive the polynomial calibration coefficients for the total pressure and dynamic pressure. The relation Eqs. (10) and (11) are a function of the computed flow yaw angle. The polynomial interpolation order is 6 and 5 for total pressure and dynamic pressure, respectively.

$$C_o = \sum_{i=0}^{n}\sum_{j=0}^{m} k_{ijt} \psi^j \theta^j \tag{10}$$

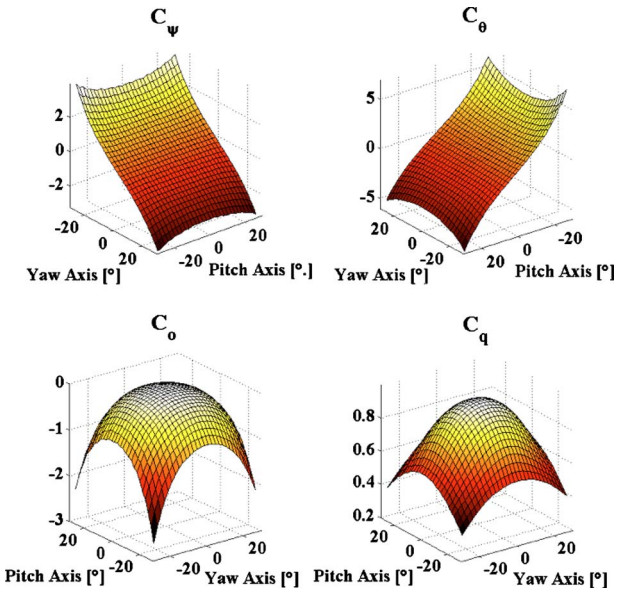

Fig. 4 Aerocalibration coefficients: (*a*) yaw flow angle, (*b*) pitch flow angle, (*c*) total pressure, and (*d*) dynamic pressure

$$C_q = \sum_{i=0}^{n}\sum_{j=0}^{m} k_{ijq} \psi^j \theta^j \tag{11}$$

The calibration curves of the 7S-FRAP probe are shown in Fig. 4 for ±30 deg in yaw and pitch, at a Mach number of Ma =0.074, which corresponds to wind dynamic head and velocity of 4 mbars and 27 m/s, respectively. Table 1 provides the calibration models uncertainties of the 7S-FRAP at Ma=0.074.

3.3 Dynamic Calibration. The pneumatic cavity between the pressure tap and the piezoresistive sensor membrane can influence the unsteady pressure measurements. The acoustic resonance is associated with the characteristic length of the pneumatic cavity, which implies that the measured signals around the eigenfrequency of the pneumatic cavity are strongly amplified and have a phase shift [18]. It is thus important to quantify the eigenfrequency of the newly design shielded pressure tap. This eigenfrequency determines the frequency measurement bandwidth of 7S-FRAP probe.

The dynamic response of the pneumatic cavity was measured in the freejet facility, equipped with a turbulence-generating fine mesh grid. The resulting flow turbulence has constant amplitude over relatively low frequencies and then decays with a characteristic slope of −5/3 at higher frequencies. The amplitude response in terms of PSD/PSD_0 versus frequency is shown in Fig. 5. The peak at 3.8 kHz corresponds with the eigenfrequency of the pneumatic cavity of the stagnation pressure sensor 7, which exhibits the largest pneumatic cavity of all seven sensors. The amplitude is flat up to a frequency of 3 kHz above which the amplitudes are in excess of 3 dB. Thus, the cutoff frequency of 3 kHz determines the bandwidth of the 7S-FRAP probe.

Table 1 Calibration model accuracy of the 7S-FRAP probe. Calibration range: Ma=0.074, ±30 deg in yaw and pitch angles.

Yaw angle abs. (deg)/rel. (%)	Pitch angle abs. (deg)/rel. (%)	Total pressure abs. (Pa)/rel. (%)	Dynamic pressure abs. (Pa)/rel. (%)
$5.75\times10^{-2}/9.58\times10^{-2}$	$5.77\times10^{-2}/9.62\times10^{-2}$	$3.93/9.58\times10^{-1}$	$2.35/5.72\times10^{-1}$

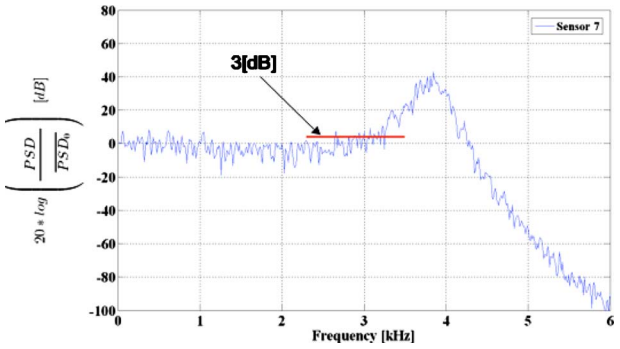

Fig. 5 Amplitude response of stagnation pressure sensor 7. The measured response is from grid generated turbulence.

3.4 Atmospheric Boundary Layer Measurements

3.4.1 Flight Plan and Measurement Approach. The atmospheric boundary layer upstream of a Vestas V80 wind turbine was measured using the seven-sensor FRAP. The wind turbine is located in Extertal, Germany. This 2.0 MW turbine has a rotor blade diameter of 80 m, with a hub height of 100 m. The cut-in and cut-out wind speeds are 4 m/s and 25 m/s, respectively. The nominal rotational speed of the rotor is 16.7 rpm and is geared up through a planetary/helical stage gearbox for electricity generation.

The vegetation and the climate of this location are representative of the "Weserbergland" region (Weser highland). The wind turbine stands at an altitude of 240 m in close proximity to a hill reaching a maximum elevation of 370 m. The orographic characteristics are complex, the landscape is characterized by a tangle of hills and valleys that drain streams into the Weser River. During the present measurement campaign, the predominant wind direction was from 340 deg north.

As shown in Fig. 6, the wind turbine is located at an area dotted with small forests and open agricultural terrain. Shown also in Fig. 6 is the plan view of the flight path of the UAV. The flight path is comprised of a 150 m long, straight, horizontally level measurement section between waypoints 1 and 2, followed by a sharp left bank turn immediately after waypoint 2, and then a more gradual left turn along an arc of a circle ahead of waypoint 1. Along this closed loop-shaped pattern, measurements were made over a height (relative to the ground) of 80–200 m, with a height resolution of 15 m. The gradual turn ahead of waypoint 2 allowed controlled ascents to be made to successive measurement

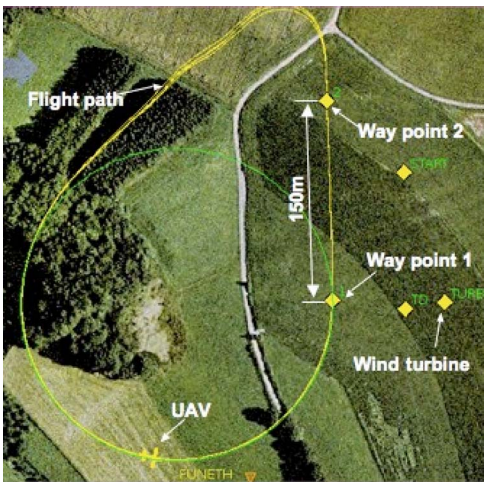

Fig. 6 Flight pattern during time-resolved wind measurements performed upstream of a Vestas V80 wind turbine

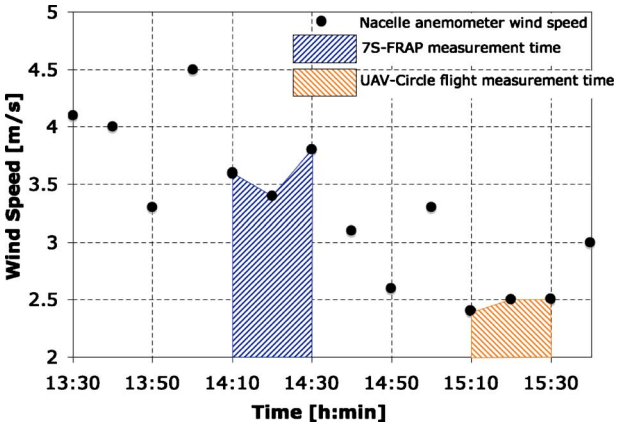

Fig. 7 The 10 min-averaged uncorrected wind speed measured by the wind turbine nacelle's anemometer. Blue- and red-dashed areas represent the 7S-FRAP and UAV circle-flight wind profile measurement time.

heights. Between waypoints 1 and 2, the UAV is flown at a constant altitude and with constant throttle. The 7S-FRAP probe thus measured the time-resolved true air speed. Therefore, the time-resolved wind velocity is derived from the difference between the true air speed and the ground speed, which is derived from the on-board GPS.

3.4.2 Measurement Results. The time-averaged wind profile measurement using the newly developed 7S-FRAP probe is compared and assessed with an independent set of measurements performed with the UAV using the more established circle-flight technique. The circle-flight measurement technique has been previously used for several atmospheric boundary layer measurement campaigns, as described by Reuder et al. [8]. The basic operating principle of the circle-flight measurement is to fly the UAV in a circular pattern such that the ground speed is decelerated by headwind on the first half of the circle and accelerated by tailwind on the other half of the circle. As the UAV is operated with constant throttle, the wind speed can be determined from the difference between minimum and maximum ground speeds over the full circle.

Figure 7 shows the 10 min-averaged wind speed that is measured on the nacelle of the wind turbine during the 7S-FRAP (20 min duration from 14:10 h to 14:30 h) and circle-flight (20 min duration from 15:10 h to 15:30 h) different measurement periods. The nacelle is equipped with an ultrasonic anemometer to measure wind speed and the uncorrected wind speed data are shown. The two sets of measurements performed upstream of the wind turbine are within 40 min time interval. The dashed blue area shows the 7S-FRAP measurement time, whereas the red-dashed indicates the UAV circle-flight measurement time. However, although the measurement periods are relatively close to each other, as shown in Fig. 7, the wind averaged velocity decreased from 3.6 m/s to 2.45 m/s between the two respective measurements. This is a challenge in making field measurements on full-scale wind turbines. Thus, at Laboratory for Energy Conversion (LEC), a subscale wind turbine facility in which model wind turbines can be tested at full-scale nondimensional in controlled conditions is used as a complement to the present paper [19].

Two measurement legs were performed during the 7S-FRAP measurement period, with 10 min interval between the two measured wind profiles. As shown in Fig. 7, the wind conditions were not similar for the three sets of wind profile measurements. Therefore, Fig. 8 shows the atmospheric boundary layer wind velocity profiles, measured by the 7S-FRAP and the UAV circle-flight techniques, nondimensionalized with the measured wind speed at 200 m. Quantitatively, the first and second 7S-FRAP profiles are

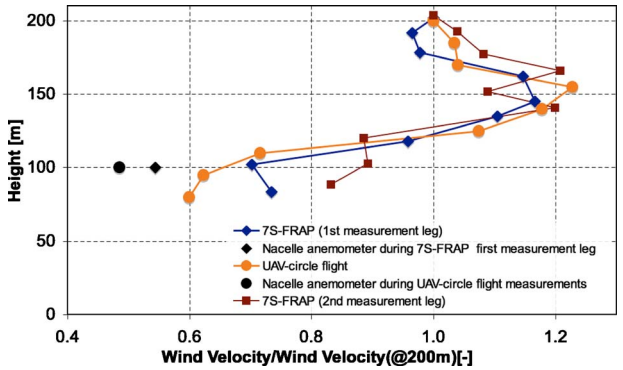

Fig. 8 Profiles of wind speed from 7S-FRAP and UAV circle-flight measurements. The nacelle anemometer averaged data are indicated with black markers. All wind velocity are nondimensionalized with the wind velocity measured at 200 m.

in a good agreement with each other, which proves a good measurement repeatability of the F7S-FRAP. The three profiles show a strong accelerated flow over the height range of 100–175 m with a peak velocity located around 150 m, which is about 20% higher than the measured wind velocity at 200 m. The wind turbine's nacelle anemometer wind velocities are also shown in Fig. 8. The uncorrected wind velocities measured at 100 m by the nacelle anemometer are of 23% and 22% lower than the 7S-FRAP first measurements and the UAV circle-flight measurements performed at 95 m and 102 m, respectively. This is in good agreement with the general assumption that a modern rotor with a maximum power coefficient of 0.45 retards the wind speed behind the rotor plane by approximately 25% [20].

Figure 9 shows the profile of the mean wind speed measured during the first measurement leg of the 7S-FRAP together with its respective maximum and minimum wind profile based on the standard deviation of the time-resolved wind speed measurements. Also shown in Fig. 9 is the logarithmic wind profile that is derived using Eq. (12). This profile is representative of a site assessment analysis in the commonly used approach of met masts equipped with cup anemometers.

$$\bar{v}_H = \bar{v}_{\text{ref}} \frac{\ln \frac{H}{z_o}}{\ln \frac{H_{\text{ref}}}{z_o}} \tag{12}$$

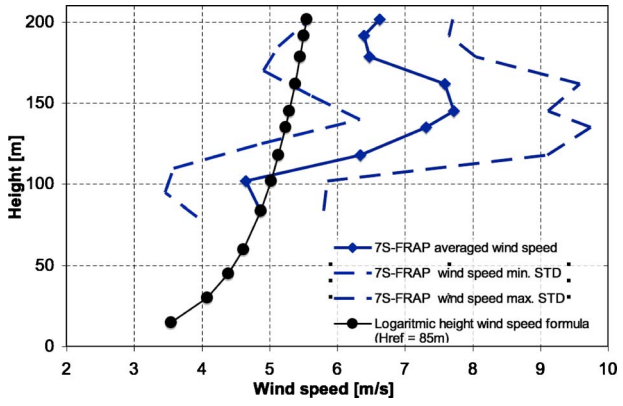

Fig. 9 Profile of wind speed measured with 7S-FRAP with its maximum and minimum wind speed based on the standard deviation of time-resolved wind speed. The black line shows the logarithmic wind profile based on the reference wind velocity measured at 85 m.

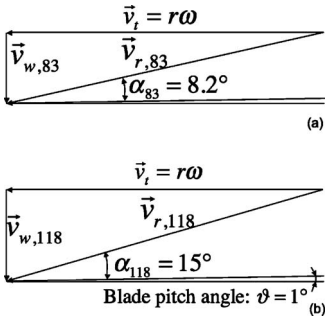

Fig. 10 Velocity triangles for a span position r/R=0.5 at (*a*) H=83 m and (*b*) H=118 m

The averaged wind speed $\bar{v}_{\text{ref}}$ measured by the 7S-FRAP at the height H_{ref}=83 m is used as a reference value. A roughness length z_o=0.15, which corresponds to roughness class of 2, has been used for the open agricultural terrain [20]. It can be observed that the logarithmic height profile gives an unsatisfactory assessment of the wind profile at this location. As the wind turbine is installed on an elevated plateau, the wind profile experiences a local acceleration, due to a venturi effect, over the heights 100–175 m approximately. The logarithmic wind profile underestimates the wind speed up to 32% at 145 m. As the wind power varies as the cube of wind speed, the estimated power is in error by up to 96%.

As shown in Fig. 9, the measured wind profile shows that there is a strong shear around the wind turbine hub height (100 m). The maximum wind speed is at 145 m and is 48% higher than the average speed at 83 m. The profile exhibits as well the highest levels of fluctuations in the range of 100–175 m, with a maximum fluctuation of 2.76 m/s at 118 m. At this height, the measured velocity fluctuations represent a 44% variation around the average speed. It can be therefore anticipated that a wind turbine at this location experiences cyclic and stochastic load variations on the turbine blades. Therefore, the design of the turbine must be capable of sustaining these load variations with time, in order that the fatigue life of the turbine components covers the expected service life.

Another consequence of the shear in the wind profile is a variation in incidence, and its associated loading, on the rotor blades. As the blade pitch is constant during a rotor revolution, the variation in velocity across the boundary layer means that the loading varies cyclically. During the 7S-FRAP measurement time, the average wind turbine rpm and the blade pitch angle were in the range of 10.5 rmp $\pm$ 0.5 rmp and 1 deg $\pm$ 0.5 deg. Figure 10 shows the velocity triangles at midspan (r/R=0.5) for heights of 83 m and 118 m. Due to the strong wind shear, the incidence changes from 8.2 deg at 83 m to 15 deg at 118 m, which are the respective bottom and top positions of the blade midspan section. The Vestas V80 wind turbine blades has a NACA 63-xxx blade profile at midspan [21]. The exact blade profile is unknown but several related reports describe studies on a NACA 63-415 or similar profiles [22]. The maximum lift coefficient for this profile is 1.5 at incidences around 13 deg. For the 118 m height, the 15 deg incidence leads to a lift coefficient of 1.28, whereas the lift coefficient at 83 m decreases to 1.13. Therefore, there is a 12% variation in the section lift between these two heights.

4 Concluding Remarks

A novel measurement approach for wind energy applications that is comprised of an autonomous UAV equipped with a seven-hole fast-response aerodynamic probe is demonstrated. The UAV is instrumented to provide autonomous flight with accurate spatial resolution (~6.3% of rotor diameter) around full-scale wind turbines. The fast-response aerodynamic probe is packaged as a com-

pact measurement system using techniques that have been developed and pioneered at ETH Zurich in its development of fast-response measurement techniques over the last 20 yrs. Static calibration of the F7S-UAV probe's sensors yield an average standard deviation of ± 2.27 Pa, which corresponds to less than 0.075% error over the full calibration range. The aerodynamic calibration yields less than 0.1% relative error in angles and total pressure, and a dynamic calibration shows that the measurement bandwidth of the present design is 3 kHz.

The time-averaged wind profile from the F7S-UAV probe is found to be in very good agreement to an independently measured wind profile. This time-averaged profile, measured in moderately complex terrain, differs by as much as 30% from a wind profile that is extrapolated from the commonly used logarithmic height formula. Analysis of the associated velocity triangles across the time-averaged profile shows that the sectional lift coefficient at the blade's midspan varies up to 12%. These variations must be accounted in the structural design of the blades. Furthermore, a comparison of the time-averaged wind speed at hub height with the wind speed measured on the wind turbine's nacelle shows that there is a 23% reduction in wind speed across the rotor, which is in very good agreement with the expected reduction for a modern wind turbine. The time-varying wind profiles show that at a given height, the velocity fluctuations vary up to 44% from the time-averaged velocity; therefore, there are substantial fluctuating loads that may impact the fatigue life of the wind turbine's components. Thus, the measurements of the unsteady wind profile accomplished with this novel measurement system demonstrate that it is a cost effective complement to the suite of available site assessment measurement tools.

Acknowledgment

The authors acknowledge the support of Thomas Künzle and Cornel Reshef, ETH Zurich, in the manufacture of the 7S-FRAP probe body and the development of the electronics, respectively. The authors also gratefully acknowledge the assistance of MM Engineering. In particular, the active support of Martin Müller in the integration of 7S-FRAP probe measurement and the Paparazzi autopilot systems, as well as his support in the conduct of the measurements, and Christian Lindenberg in the construction of the UAV airframe and services as a safety pilot during the measurement campaign. The authors thank PNE Wind AG for providing access to the wind turbine and its performance data, and, in particular, Mr. Eliert Nickaes for his enthusiastic and ongoing interest for the project.

Nomenclature

h = hour
min = minute
p = pressure
r = radial potion
t = time
v = absolute velocity
z_o = roughness factor
H = height
K = polynomial coefficient
R = turbine blade radius
U = voltage
T = temperature

Greek

α = incidence angle
θ = pitch angle
ψ = yaw angle
ω = angular velocity

Superscript

$\bar{}$ = average

Subscripts

83 = 83 m height
118 = 118 m height
e = excitation
f = freestream
max = maximum
min = minimum
o = total
q = dynamic head
r = relative
ref = reference condition
t = tangential
w = wind
x = axial direction

Abbreviations

ADC = analog-to-digital converter
LIDAR = light detection and ranging
PSD = power spectral density
UAV = uninhabited aerial vehicle
7S-FRAP = seven-sensor fast-response aerodynamic probe

References

[1] Kristensen, L., 1999, "The Perennial Cup Anemometer," Wind Energy, **2**, pp. 59–75.
[2] Courtney, M., Wagner, R., and Lindelöw, P., 2008, "Testing and Comparison of Lidars for Profile and Turbulence Measurements in Wind Energy," IOP Conf. Series: Earth and Environmental Science, **1**, p. 012021.
[3] Frehlich, R., and Kelley, N., 2008, "Measurements of Wind and Turbulence Profiles With Scanning Doppler Lidar for Wind Energy Applications," IEEE J. Sel. Top. Appl. Earth Observations and Remote Sensing, **1**, pp. 42–47.
[4] Smith, D. A., Harris, M., Coffey, A. S., Mikkelsen, T., Joergensen, H. E., Mann, J., and Danielan, R., 2004, "Wind Lidar Evaluation at the Danish Wind Test Site in Hovsore," EWEC 2004, London.
[5] Hannon, S., Barr, K., Novotny, J., Bass, J., Oliver, A., and Anderson, M., 2008, "Large Scale Wind Resource Mapping Using a State-of-the-Art 3D Scanning LIDAR," European Wind Energy Conference and Exhibition, Brussels, Belgium, Mar. 31–Apr. 3, pp. 1–7.
[6] Mikkelsen, T., Mann, J., Courtney, M., and Sjöholm, M., 2008, "Windscanner: 3-D Wind and Turbulence Measurements From Three Steerable Doppler Lidars," IOP Conf. Series: Earth and Environmental Science, **1**, p. 012018.
[7] Spiess, T., Bange, J., Buschmann, M., and Vörsmann, P., 2007, "First Application of the Meteorological Mini-UAV 'M^{2}AV'," Meteorol. Z., **16**, pp. 159–169.
[8] Reuder, J., Brisset, P., Jonassen, M., Mueller, M., and Mayer, S., 2008, "SUMO: A Small Unmanned Meteorological Observer for Atmospheric Boundary Layer Research," IOP Conf. Series: Earth and Environmental Science, **1**, p. 012014.
[9] Kupferschmied, K., Köppel, P., Roduner, C., and Gyarmathy, G., 2000, "On the Development and Application of the Fast-Response Aerodynamic Probe System in Turbomachines—Part 1: The Measurement System," ASME J. Turbomach., **122**, pp. 505–516.
[10] Pfau, A., Schlienger, J., Kalfas, A. I., and Abhari, R. S., 2002, "Virtual Four Sensor Fast Response Aerodynamic Probe (FRAP)," 16th Bi-Annual Symposium on Measuring Techniques in Transonic and Supersonic Flows in Cascades and Turbomachines, Cambridge, UK, Sep. 23–24.
[11] Porreca, L., Hollenstein, M., Kalfas, A., and Abhari, R., 2007, "Turbulence Measurements and Analysis in a Multistage Axial Turbine," J. Propul. Power, **23**, pp. 227–234.
[12] Mansour, M., Chokani, N., Kalfas, A. I., and Abhari, R. S., 2008, "Time-Resolved Entropy Measurements Using a Fast Response Entropy Probe," Meas. Sci. Technol., **19**(11), p. 115401.
[13] Bryer, D. W., and Pankhurst, R. C., 1971, *Pressure-Probe Methods for Determining Wind Speed and Flow Direction*, Her Majesty's Stationary Office, London.
[14] Brisset, P., Drouin, A., Gorraz, M., Huard, P.-S., and Tyler, J., 2006, "The Paparazzi Solution," MAV2006, Sandestin, FL.
[15] Mueller, M., and Drouin, A., 2007, "Paparazzi—The Free Autopilot. Build Your Own UAV," 24th Chaos Communication Congress, Berliner Congress Center, Dec. 27–30.
[16] Zilliac, G. G., 1993, "Modelling, Calibration, and Error Analysis of Seven-Hole Pressure Probes," Exp. Fluids, **14**, pp. 104–120.
[17] Gallington, R. W., 1980, "Measurement of Very Large Flow Angles With Non-Nulling Seven-Hole Probe," Aeronautics Digest, Vol. USAFA-TR-80-17, pp. 60–88.
[18] Gossweiler, C., Humm, H. J., and Kupefrschmied, P., 1989, "The Use of Piezo-Resistive Semi-Conductor Pressure Transducers for Fast-Response Probe Measurements in Turbomachinery," *Proceedings of the Tenth Symposium on Measuring Techniques for Transonic and Supersonic Flows in Cascades and Turbomachines*, Brussel.

[19] Barber, S., Wang, Y., Chokani, N., and Abhari, R. S., 2009, "The Effect of Ice Shapes on Wind Turbine Performance," 13th International Workshop on Atmospheric Icing of Structures, Andermatt, Switzerland.
[20] Hau, E., 2006, *Wind Turbines: Fundamentals, Technologies, Applications, Economics*, Springer-Verlag, Berlin.
[21] Hochart, C., 2007, "Simulation Numérique et Expérimentale de l'Ecoulement d'Air et de l'Accrétion de Glace autour d'une Pale d'Eolienne," MS thesis, Univérsité de Québec.
[22] Bak, C., Fuglsang, P., Johansen, J., and Antoniou, I., 2000, "Wind Tunnel Tests of the NACA 63-415 and a Modified NACA 64-415," Risø National Laboratory, Roskilde, Denmark.